

2422 **Chapter 9**
2423 **Weak Focusing Synchrotron**

2424 **Abstract** This Chapter introduces to the weak focusing synchrotron, and to the the-
2425 oretical material needed for the simulation exercises. It begins with a brief reminder
2426 of the historical context, and continues with beam optics and acceleration techniques
2427 which the weak synchrotron principle and methods lean on. Regarding the latter, it
2428 relies on basic charged particle optics and acceleration concepts introduced in the
2429 previous Chapters, and further addresses the following aspects:

- 2430 - fixed closed orbit,
- 2431 - periodic structure,
- 2432 - periodic motion stability,
- 2433 - optical functions,
- 2434 - synchrotron motion,
- 2435 - depolarizing resonances.

2436 The simulation of weak synchrotrons only require a very limited number of optical
2437 elements; actually two are enough: DIPOLE or BEND to simulate combined function
2438 dipoles, and DRIFT to simulate straight section. A third one CAVITE, is required
2439 for acceleration. Particle monitoring requires keywords introduced in the previous
2440 Chapters, including FAISCEAU, FAISTORE, possibly PICKUPS, and some others.
2441 Spin motion computation and monitoring resort to SPNTRK, SPNPRT, FAISTORE.
2442 Optics matching and optimization use FIT[2]. SYSTEM again is used to shorten the
2443 input data files.

2444 **Notations used in the Text**

| | |
|---------------------------------------|---|
| $B; \mathbf{B}, B_{x,y,s}$ | field value; field vector, its components in the moving frame |
| $B\rho = p/q; B\rho_0$ | particle rigidity; reference rigidity |
| $C; C_0$ | orbit length, $C = 2\pi R + \left[\begin{array}{l} \text{straight} \\ \text{sections} \end{array} \right]$; reference, $C_0 = C(p = p_0)$ |
| E | particle energy |
| EFB | Effective Field Boundary |
| $f_{\text{rev}}, f_{\text{rf}}$ | revolution and accelerating voltage frequencies |
| h | RF harmonic number, $h = f_{\text{rf}}/f_{\text{rev}}$ |
| $m; m_0; M$ | mass, $m = \gamma m_0$; rest mass; in units of MeV/c ² |
| $n = \frac{\rho}{B} \frac{dB}{d\rho}$ | focusing index |
| $\mathbf{p}; p; p_0$ | momentum vector; its modulus; reference |
| P_i, P_f | polarization, initial, final |
| q | particle charge |
| r, R | orbital radius ; average radius, $R = C/2\pi$ |
| s | path variable |
| v | particle velocity |
| 2445 $V(t); \hat{V}$ | oscillating voltage; its peak value |
| x, x', y, y' | horizontal and vertical coordinates in the moving frame |
| α | momentum compaction, or trajectory deviation |
| $\beta = v/c; \beta_0; \beta_s$ | normalized particle velocity; reference; synchronous |
| β_u | betatron functions ($u : x, y, Y, Z$) |
| $\gamma = E/m_0$ | Lorentz relativistic factor |
| $\Delta p, \delta p$ | momentum offset |
| ε | wedge angle |
| ε_u | Courant-Snyder invariant ($u : x, r, y, l, Y, Z, s$, etc.) |
| ε_R | strength of a depolarizing resonance |
| μ_u | betatron phase advance, $\mu_u = \int_{\text{period}} ds/\beta_u(s)$ ($u : x, y, Y, Z$) |
| ν_u | wave number or “tune”, radial, vertical, synchrotron ($u : x, y, Y, Z, l$) |
| ρ | curvature radius |
| $\phi; \phi_s$ | particle phase at voltage gap; synchronous phase |
| ϕ_u | betatron phase advance, $\phi_u = \int ds/\beta_u$ ($u : x, y, Y, \text{or } Z$) |
| φ | spin angle to the vertical axis |

2446 **Introduction**

2447 The synchrotron is an outcome of the mid-1940s longitudinal phase focusing syn-
 2448 chronous acceleration concept [1, 2]. In its early version, transverse beam stability
 2449 in the synchrotron during the thousands of turns that the acceleration lasts was based
 2450 on the technique known at the time: weak focusing, as in the cyclotron and in the be-
 2451 tatron. An existing betatron was used to first demonstrate phase-stable synchronous

2452 acceleration with slow variation of the magnetic field, on a fixed orbit, in 1946 [3],
 2453 - closely following the demonstration of the principle of phase focusing using a
 2454 fixed-field cyclotron [4].

2455 Phase focusing states that stability of the longitudinal motion, longitudinal focus-
 2456 ing, is obtained if particles in a bunch, which have a natural energy spread, arrive
 2457 at the accelerating gap in the vicinity of a proper phase of the oscillating voltage,
 2458 the synchronous phase; if this condition is fulfilled the bunch stays together, in the
 2459 vicinity of the latter, during acceleration. Synchrotrons operate in general in a non-
 2460 isochronous regime: the revolution period changes with energy; as a consequence,
 2461 in order to maintain an accelerated bunch on the synchronous phase, the RF voltage
 2462 frequency, which satisfies $f_{rf} = h f_{rev}$, has to change continuously from injection to
 2463 top energy. The reference orbit in a synchrotron is maintained at constant radius by
 2464 ramping the guiding field in the main dipoles in synchronism with the acceleration,
 2465 as in the betatron [5].

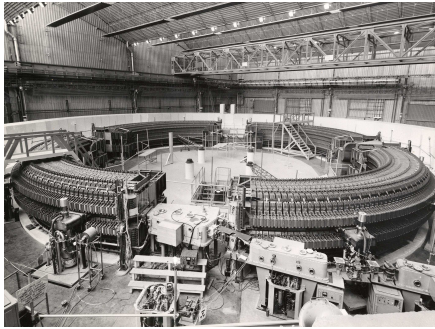


Fig. 9.1 Saturne I at Saclay [6], a 3 GeV, 4-period, 68.9 m circumference, weak focusing synchrotron, constructed in 1956-58. The injection line can be seen in the foreground, injection is from a 3.6 MeV Van de Graaff (not visible)

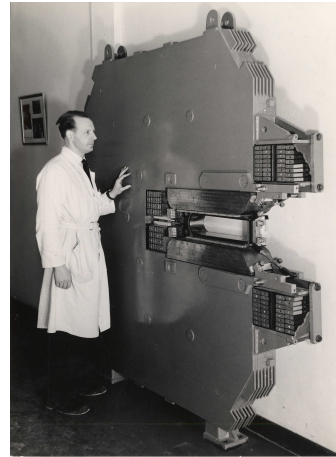


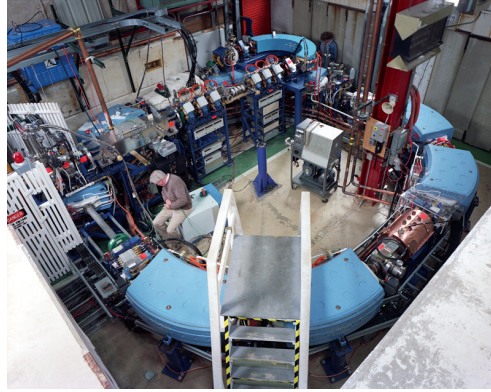
Fig. 9.2 A slice of Saturne I dipole [7]. The slight gap tapering is hardly visible (increasing outward), it determines the weak index condition $0 < n < 1$

2466 The synchrotron concept allowed the highest energy reach by particle accelerators
 2467 at the time, it led to the construction of a series of proton rings with increasing
 2468 energy [8]: 1 GeV at Birmingham (1953), 3.3 GeV at the Cosmotron (Brookhaven
 2469 National Laboratory, 1953-1969), 6.2 GeV at the Bevatron (Berkeley, 1954-1993),
 2470 10 GeV at the Synchro-Phasotron (JINR, Dubna, 1957-2003), and a few additional
 2471 ones in the late 1950s well into the era of the concept which would essentially
 2472 dethrone the weak focusing method and its quite bulky rings of magnets which were
 2473 a practical limit to further increase in energy¹: the strong focusing synchrotron (the

¹ The story has it that it is possible to ride a bicycle in the vacuum chamber of Dubna's Synchro-Phasotron.

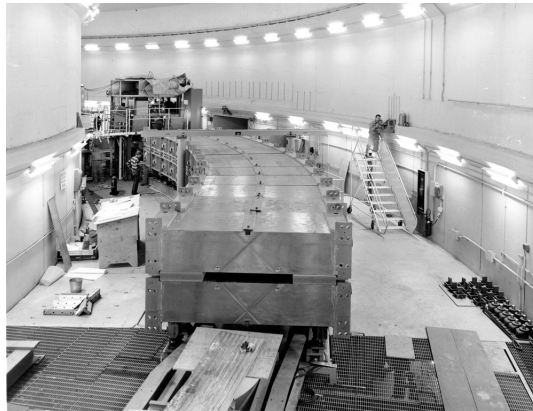
2474 object of Chapter 10). The general layout of these first weak focusing synchrotrons
 2475 included straight sections (often 4, Fig. 9.1), which allowed insertion of injection
 2476 (Fig. 9.1) and extraction systems, accelerating cavities, orbit correction and beam
 2477 monitoring equipment.

Fig. 9.3 Left: Loma Linda University medical synchrotron, during commissioning in 1989 at the Fermilab National Laboratory where it was designed and constructed [9]



2478 The next decades following the invention of the synchrotron saw applications in
 2479 many fields of science including fixed-target nuclear physics for particle discovery,
 2480 material science, medicine, industry. Its technological simplicity still makes it an
 2481 appropriate technology today in low energy beam application when relatively low
 2482 current is not a concern, as in the hadrontherapy application (Fig. 9.3) [10, 11]: it
 2483 essentially requires a single type of a simple dipole magnet, an accelerating gap, some
 2484 command-control instrumentation, whereas it procures greater beam manipulation
 2485 flexibilities compared to (synchro-)cyclotrons.

Fig. 9.4 The ZGS at Argonne during construction. A 12 GeV, 8-dipole, 4-period, 172 m circumference, wedge focusing synchrotron. The two persons inside and outside the ring, in the background, give an idea of the size of the magnets



2486 *Polarized beams*

2487 The availability of polarized proton sources allowed the acceleration of polarized
 2488 beams to high energy. The possibility was considered from the early times at Argonne
 2489 ZGS (Zero-Gradient Synchrotron), a 12 GeV weak focusing synchrotron operated
 2490 over 1964-1979 [12] (Fig. 9.4). Up to 70% polarization transmission through the
 2491 synchrotron was achieved, for the first time in a synchrotron² and reaching multi-GeV
 2492 energy in 1973, up to 17.5 GeV/c with *appreciable polarizations* [13]. Polarization
 2493 preservation techniques included harmonic orbit correction and betatron tune jump
 2494 at strongest depolarizing resonances (Fig. 9.15). Experiments were performed to
 2495 assess the possibility of polarization transmission in strong focusing synchrotrons,
 2496 and polarization lifetime in colliders [14]. Acceleration of polarized deuteron was
 2497 achieved in the late 1970s, when sources were made available [15].

2498 **9.1 Basic Concepts and Formulae**

2499 The synchrotron is based on two key principles. On the one hand, a slowly varying
 2500 magnetic field to maintain a constant orbit during acceleration,

$$B(t) \times \rho = p(t)/q, \quad \rho = \text{constant}, \quad (9.1)$$

2501 with $p(t)$ the particle momentum and ρ the bending radius in the dipoles. On the other
 2502 hand, on synchronous acceleration for longitudinal phase stability. In a regime where
 2503 the velocity change with energy cannot be ignored (non-ultrarelativistic particles),
 2504 the latter requires a modulation of the accelerating voltage frequency so to satisfy

$$f_{RF}(t) = hf_{rev}(t) \quad (9.2)$$

2505 Synchronism between accelerating voltage oscillation and the revolution motion
 2506 keeps the bunch on the synchronous phase at traversal of the accelerating gaps.
 2507 Synchronous acceleration is technologically simpler in the case of electrons, as
 2508 frequency modulation is unnecessary beyond a few MeV; for instance, from $v/c =$
 2509 0.9987 at 10 MeV to $v/c \rightarrow 1$ the relative change in revolution frequency amounts
 2510 to $\delta f_{rev}/f_{rev} = \delta\beta/\beta < 0.0013$.

2511 These are two major evolutions compared to the cyclotron, where, instead, the
 2512 magnetic field is fixed - the reference orbit spirals out, and, by virtue of the isochro-
 2513 nism of the orbits, the oscillating voltage frequency is fixed as well.

2514 A fixed orbit reduces the radial extent of individual guiding magnets, allowing a
 2515 ring structure comprised of a circular string of dipoles. For the sake of comparison:
 2516 a synchrocyclotron instead uses a single, massive dipole; increased energy requires
 2517 increased radial extent of the magnet to allow for the greater bending field integral

² Polarized beam had been accelerated in cyclotrons, at earlier times.

2518 (*i.e.*, $\oint B dl = 2\pi R_{max} \hat{B} = p_{max}/q$), thus a volume of iron increasing more than
 2519 quadratically with bunch rigidity.

2520 One or the other of the weak index ($-1 < k < 0$, Sect. 4.2.2) and/or wedge
 2521 focusing (Sect. 18.3.1) are used in weak focusing synchrotrons. Transverse stability
 2522 was based on the latter at Argonne ZGS (Zero-Gradient Synchrotron: the main
 2523 magnet had no field index); ZGS accelerated polarized proton beams, weak focusing
 2524 resulted in weak depolarizing resonances, an advantage in that matter [14].

2525 Due to the necessary ramping of the field in order to maintain a constant orbit,
 2526 the synchrotron is a pulsed accelerator, the acceleration is cycled, from injection to
 2527 top energy, repeatedly. The repetition rate of the acceleration cyclic depends on the
 2528 type of power supply. If the ramping uses a constant electromotive force ($E=V+ZI$
 2529 is constant), then

$$B(t) \propto (1 - e^{-t/\tau}) = 1 - \left[1 - \left(\frac{t}{\tau}\right) + \left(\frac{t}{\tau}\right)^2 - \dots \right] \approx \frac{t}{\tau} \quad (9.3)$$

2530 essentially linear. In that case $\dot{B} = dB/dt$ does not exceed a few Tesla/second, thus the
 2531 repetition rate of the acceleration cycle is of the order of a Hertz. If instead the magnet
 2532 winding is part of a resonant circuit (with typically 10 ~ 60 Hz eigenfrequency) the
 2533 field oscillate,

$$B(t) = B_0 + \frac{\hat{B}}{2}(1 - \cos \omega t) \quad (9.4)$$

2534 so that, in the interval of half a voltage repetition period (*i.e.*, $t : 0 \rightarrow \pi/\omega$) the
 2535 field increases from an injection threshold value to a maximum value at highest
 2536 rigidity, $B(t) : B_0 \rightarrow B_0 + \hat{B}$. The latter determines the highest achievable energy:
 2537 $\hat{E} = pc/\beta = q\hat{B}\rho c/\beta$. The repetition rate with resonant magnet cycling can reach a
 2538 few tens of Hertz, a species known as “rapid-cycling” synchrotrons. In both cases
 2539 anyway B imposes its law and the other quantities comprising the acceleration cycle
 2540 (RF frequency in particular) will follow B(t).

2541 For the sake of comparison: in a synchrocyclotron the field is constant, thus
 2542 acceleration can be cycled as fast as the swing of the voltage frequency allows
 2543 (hundreds of Hz are common practice); assume a conservative 10 kVolts per turn,
 2544 thus of the order of 10,000 turns to 100 MeV, with velocity $0.046 < v/c < 0.43$
 2545 from 1 to 100 MeV, proton. Take $v \approx 0.5c$ to make it simple, an orbit circumference
 2546 below 30 meter, thus the acceleration takes of the order of $10^4 \times C/0.5c \approx$ ms range,
 2547 potentially a repetition rate in kHz range, more than an order of magnitude beyond
 2548 the reach of a rapid-cycling pulsed synchrotron.

2549 9.1.1 Periodic Stability

2550 This section introduces the various components of the transverse focusing and the
 2551 conditions for periodic stability in a weak focusing synchrotron. It builds on material
 2552 introduced in Chap. 4, Classical Cyclotron, and on Ref. [16].

2553 **9.1.1.1 Closed orbit**

2554 The concept is found in the betatron, which accelerates particles on a constant orbit
 2555 (Chap. 7). The closed orbit is fixed, and maintained during acceleration by ensuring
 2556 that the relationship Eq. 9.1 is satisfied. In a perfect ring, the closed orbit is along an
 2557 arc in the bending magnets and straight along the drifts, Fig. 9.5.

2558 Particle motion is defined in a moving frame (O;s,x,y) whose origin coincides
 2559 with the location of an ideal particle following the reference orbit. The moving frame
 2560 s axis is tangent to the reference orbit, its transverse horizontal axis x is normal to
 2561 the s axis, its vertical axis y is normal to the (s, x) plane (Fig. 4.8, Sect. 4.2.2).

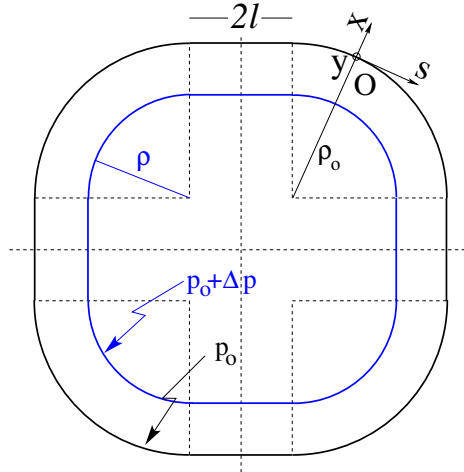


Fig. 9.5 A $2\pi/4$ axially symmetric structure with four drift spaces. Orbit length on reference momentum p_0 is $C = 2\pi\rho_0 + 8l$. (O;s,x,y) is the moving frame, along the reference orbit. The orbit for momentum $p = p_0 + \Delta p$ ($\Delta p < 0$, here) is at constant distance $\Delta x = \frac{\rho_0}{1-n} \frac{\Delta p}{p_0} = \frac{R}{(1+k)(1-n)} \frac{\Delta p}{p_0}$ from the reference orbit

2562 **9.1.1.2 Transverse Focusing**

2563 Radial motion stability around a reference closed orbit in an axially symmetric dipole
 2564 field requires a field index (Sect. 4.2.2),

$$n = -\frac{\rho_0}{B_0} \left. \frac{\partial B_y}{\partial x} \right|_{x=0, y=0} \tag{9.5}$$

2565 a quantity evaluated on the reference arc in the dipoles, satisfying the weak focusing
 2566 condition

$$0 < n < 1 \tag{9.6}$$

2567 This condition can be obtained with a tapered gap (Fig. 9.2) causing the magnetic
 2568 field to decrease slowly with radius, so resulting in both axial and radial focusing

2569 (Figs. 9.6, 9.7). Note the sign convention here, the cyclotron uses the opposite sign
 2570 (Eq. 4.10). This condition holds regardless of the presence of drifts or not. Adding
 2571 drift spaces between the dipoles, the reference orbit is comprised of arcs of radius
 2572 ρ_0 in the magnets, and straight segments along the drift spaces that connect these
 2573 arcs. This requires defining two radii, namely,

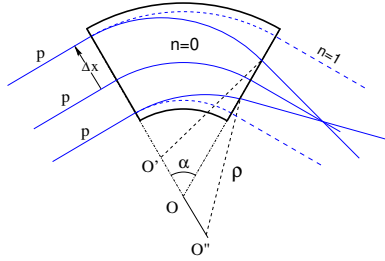


Fig. 9.6 Geometrical focusing: in a sector dipole with focusing index $n = 0$, parallel incoming rays of equal momenta experience the same curvature radius ρ , their trajectories converge as outer trajectories have a longer path in the field, compared to inner ones. An index value $n=1$ cancels that effect: rays exit parallel

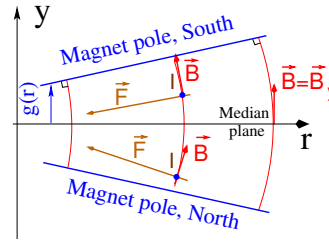


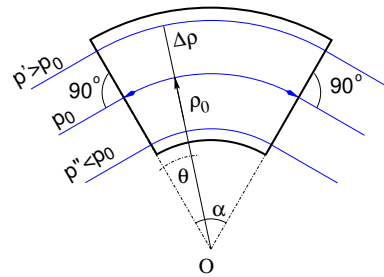
Fig. 9.7 Axial motion stability requires proper shaping of field lines: B_y has to decrease with radius. The Laplace force pulls a positive charge with velocity pointing out of the page, at I, toward the median plane. Increasing the field gradient (n closer to 1, gap opening up faster) increases the focusing

- 2574 (i) the magnet curvature radius ρ_0 ,
- 2575 (ii) an average radius $R = C/2\pi = \rho_0 + Nl/\pi$ (with C the length of the reference
 2576 closed orbit and $2l$ the drift length) (Fig. 9.5) which also writes

$$R = \rho_0(1 + k), \quad k = \frac{Nl}{\pi\rho_0} \quad (9.7)$$

2577 Adding drift spaces decreases the average focusing around the ring.

Fig. 9.8 In a sector dipole with radial index $n \neq 0$, closed orbits follow arcs of constant field. A closed orbit at $p_0 + \Delta p$ follows an arc of radius $\rho_0 + \Delta\rho$, $\Delta\rho = \Delta p/(1 + n)qB_0$



2578 *Geometrical focusing*

2579 The limit $n \rightarrow 1$ of the transverse motion stability domain corresponds to a cancel-
 2580 lation of the geometrical focusing (Fig. 9.6): in a constant field dipole (radial field
 2581 index $n=0$) the longer (respectively shorter) path in the magnetic field for parallel
 2582 trajectories entering the magnet at greater (respectively smaller) radius result in
 2583 convergence. This effect is cancelled, *i.e.*, the deviation is the same whatever the
 2584 entrance radius, if the curvature center is made independent of the entrance radius:
 2585 $OO' = 0$, $O''O = 0$. This occurs if trajectories at an outer (inner) radius experience a
 2586 smaller (greater) field such as to satisfy $BL = B\rho\alpha = C^{st}$. Differentiating $B\rho = C^{st}$
 2587 gives $\frac{\Delta B}{B} + \frac{\Delta\rho}{\rho} = 0$, with $\Delta\rho = \Delta x$, so yielding $n = -\frac{\rho_0}{B_0} \frac{\Delta B}{\Delta x} = 1$. The focal distance
 2588 associated with the curvature is (Eq. 4.12 with $R = \rho_0$) $f = \frac{\rho_0^2}{L}$. Optical drawbacks
 2589 of the weak focusing method include the weakness of the focusing and the absence
 2590 of independent radial and axial focusing.

2591 *Wedge Focusing*

2592 Entrance and exit wedge angles may be used to ensure transverse focusing: opening
 2593 the magnetic sector increases the horizontal focusing (and decreases the vertical
 2594 focusing); closing the magnetic sector has the reverse effect (Sect. 18.3.1). In a point
 2595 transform approximation, at the wedge the trajectory undergoes a local deviation
 2596 proportional to the distance to the optical axis, namely,

$$\Delta x' = \frac{\tan \varepsilon}{\rho_0} \Delta x, \quad \Delta y' = -\frac{\tan(\varepsilon - \psi)}{\rho_0} \Delta y \quad (9.8)$$

2597 ψ is a correction for the fringe field extent (Eq. 18.23), an effect on the vertical
 2598 focusing of the first order in the coordinates (it is a second order effect horizontally).

2599 Profiling the magnet gap in order to adjust the focal distance complicates the
 2600 magnet; a parallel gap, $n = 0$, makes it simpler, for that reason edge focusing may
 2601 be preferred. Wedge vertical focusing in the ZGS ($\varepsilon > 0$) was at the expense of
 2602 horizontal geometrical focusing (Fig. 9.8). This was an advantage though, for the
 2603 acceleration of polarized beams, as radial field components (which are responsible for
 2604 depolarization) were only met at the EFBs of the eight main dipoles [13]. Preserving
 2605 beam polarization at high energy required tight control of the tunes, and this was
 2606 achieved by, in addition, pole face windings at the ends of the dipoles [17, 18];
 2607 these coils were pulsed to control the amplitude detuning, resulting in a control
 2608 of the tunes at 0.01 level; they also compensated eddy current induced sextupole
 2609 perturbations which affected the vertical tune.

2610 **9.1.1.3 Periodic stability, betatron motion**

2611 The first order differential equations of motion in the moving frame (Fig. 9.5) derive
2612 from the Lorentz equation [16]

$$\frac{dm\mathbf{v}}{dt} = q\mathbf{v} \times \mathbf{B} \Rightarrow m \frac{d}{dt} \begin{Bmatrix} \frac{ds}{dt} \mathbf{s} \\ \frac{dx}{dt} \mathbf{x} \\ \frac{dy}{dt} \mathbf{y} \end{Bmatrix} = q \begin{Bmatrix} (\frac{dx}{dt} B_y - \frac{dy}{dt} B_x) \mathbf{s} \\ -\frac{ds}{dt} B_y \mathbf{x} \\ \frac{ds}{dt} B_x \mathbf{y} \end{Bmatrix} \quad (9.9)$$

2613 Introduce the field index $n = -\frac{\rho_0}{B_0} \frac{\partial B_y}{\partial x}$ evaluated on the reference orbit, with $B_0 =$
2614 $B_y(\rho_0, y = 0)$; assume transverse stability: $0 < n < 1$. Taylor expansion of the
2615 transverse field components in the moving frame write

$$\begin{aligned} B_y(\rho) &= B_y(\rho_0) + x \left. \frac{\partial B_y}{\partial x} \right|_{\rho_0} + \mathcal{O}(x^2) \approx B_y(\rho_0) - n \frac{B_y}{\rho_0} \Big|_{\rho_0} x = B_0(1 - n \frac{x}{\rho_0}) \\ B_x(0 + y) &= \underbrace{B_x(0)}_{=0} + y \underbrace{\left. \frac{\partial B_x}{\partial y} \right|_{\rho_0}}_{= \frac{\partial B_y}{\partial x}} + (\text{higher order in } y) \approx -n \frac{B_0}{\rho_0} y \end{aligned} \quad (9.10)$$

2616 Introduce in addition $ds \approx vdt$, Eqs. 9.9, 9.10 lead to the differential equations of
2617 motion in a dipole field

$$\frac{d^2 x}{ds^2} + \frac{1-n}{\rho_0^2} x = 0, \quad \frac{d^2 y}{ds^2} + \frac{n}{\rho_0^2} y = 0 \quad (9.11)$$

2618 It results that, in an S-periodic structure comprised of gradient dipoles, wedges
2619 and drift spaces, the differential equation of motion takes the general form of Hill's
2620 equation, a second order differential equation with periodic coefficient, namely (with
2621 u standing for x or y),

$$\begin{cases} \frac{d^2 u}{ds^2} + K_u(s)u = 0 \\ K_u(s+S) = K_u(s) \end{cases} \quad \text{with} \quad \begin{cases} \text{in dipoles : } \begin{cases} K_x = (1-n)/\rho_0^2 \\ K_y = n/\rho_0^2 \end{cases} \\ \text{at a wedge : } K_{\frac{x}{y}} = \pm(\tan \varepsilon)/\rho_0 \\ \text{in drift spaces : } K_x = K_y = 0 \end{cases} \quad (9.12)$$

2622 $K_u(s)$ is S-periodic, $S = 2\pi R/N$ ($S = C/4$ for instance in a 4-periodic ring,
2623 Figs. 9.1, 9.5).

2624 The solution of Eqs. 9.12 is not as straightforward as in the cyclotron where K_u is
2625 constant around the ring (Eq. 4.13), which results in a sinusoidal motion (Eq. 4.15)
2626 - the latter is on the other hand a reasonable approximation, see below, *Weak focusing*
2627 *approximation*. G. Floquet has established [19] that the two independent solutions
2628 of Hill's second order differential equation have the form [16]

$$\begin{cases} u_1(s) = \sqrt{\beta_u(s)} e^{i \int_0^s \frac{ds}{\beta_u(s)}} \\ du_1(s)/ds = \frac{i - \alpha_u(s)}{\beta_u(s)} u_1(s) \end{cases} \quad \text{and} \quad \begin{cases} u_2(s) = u_1^*(s) \\ du_2(s)/ds = du_1^*(s)/ds \end{cases} \quad (9.13)$$

2629 wherein $\beta_u(s)$ and $\alpha_u(s) = -\beta'_u(s)/2$ are S-periodic functions, from what it results
2630 that

$$u_{\frac{1}{2}}(s+S) = u_{\frac{1}{2}}(s) e^{\pm i \mu_u} \quad (9.14)$$

2631 wherein

$$\mu_u = \int_{s_0}^{s_0+S} \frac{ds}{\beta_u(s)} \quad (9.15)$$

2632 is the betatron phase advance over a period. A real solution of Hill's equation is the
2633 linear combination $A u_1(s) + A^* u_2^*(s)$. With $A = \frac{1}{2} \sqrt{\varepsilon_u/\pi} e^{i\phi}$ following conventional
2634 notations, the general solution of Eq. 9.12 then writes

$$\begin{cases} u(s) = \sqrt{\beta_u(s)\varepsilon_u/\pi} \cos\left(\int \frac{ds}{\beta_u} + \phi\right) \\ u'(s) = -\sqrt{\frac{\varepsilon_u/\pi}{\beta_u(s)}} \sin\left(\int \frac{ds}{\beta_u} + \phi\right) + \alpha_u(s) \cos\left(\int \frac{ds}{\beta_u} + \phi\right) \end{cases} \quad (9.16)$$

2635 An invariant of the motion is

$$\frac{1}{\beta_u(s)} [u^2 + (\alpha_u(s)u + \beta_u(s)u')^2] = \frac{\varepsilon_u}{\pi} \quad (9.17)$$

2636 known as the Courant-Snyder invariant. At a given azimuth s of the periodic structure
2637 the observed turn-by-turn motion lies on that ellipse (Fig. 9.9). The form and
2638 inclination of the ellipse depend on the observation azimuth s via the respective local
2639 values of $\alpha_u(s)$ and $\beta_u(s)$, but its surface ε_u is invariant. Motion along the ellipse
2640 is clockwise, as can be figured from Eq. 9.16 considering an observation azimuth
 s where the ellipse is upright, $\alpha_u(s) = 0$. In an N-periodic ring, the phase advance

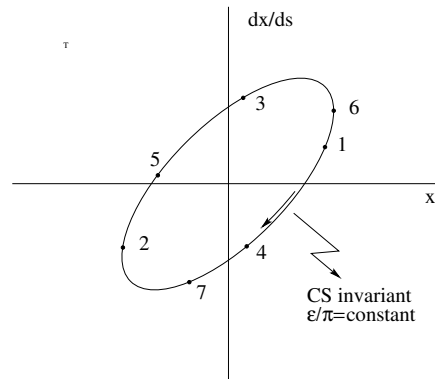


Fig. 9.9 Courant-Snyder invariant and turn-by-turn harmonic motion along the invariant, observed at some azimuth s . The form of the ellipse depends on the observation azimuth s but its surface ε_u is invariant

2641 over a turn (from one location to the next on the ellipse in Fig. 9.9) is

$$\int_{s_0}^{s_0+NS} \frac{ds}{\beta_u(s)} = N \int_{\text{period}} \frac{ds}{\beta_u(s)} = N\mu_u \quad (9.18)$$

2642 *Weak focusing approximation*

2643 In the case of a cylindrically symmetric structure, a sinusoidal motion is the exact
 2644 solution of the first order differential equations of motion (Eqs. 4.14, 4.15, Classical
 2645 Cyclotron Chapter). In that case the latter have a constant (s-independent) coefficient,
 2646 $K_x = (1 - n)/R_0^2$ and $K_y = n/R_0^2$, respectively. Adding drift spaces results in Hill's
 2647 differential equation with periodic coefficient $K(s + S) = K(s)$ (Eq. 9.12), and in a
 2648 pseudo harmonic solution (Eq. 9.16). Due to the weak focusing the beam envelope
 2649 is only weakly modulated (see below), thus so is $\beta_u(s)$. In a practical manner, the
 2650 modulation of $\beta_u(s)$ does not exceed a few percent, this justifies introducing the
 2651 average value $\bar{\beta}_u$ to approximate the phase advance by

$$\int_0^s \frac{ds}{\beta_u(s)} \approx \frac{s}{\bar{\beta}_u} = \nu_u \frac{s}{R} \quad (9.19)$$

2652 The right equality is obtained by applying this approximation to the phase advance
 2653 per period (Eq. 9.15), namely $\mu_u = \int_{s_0}^{s_0+S} \frac{ds}{\beta_u(s)} \approx S/\bar{\beta}_u$, and introducing the wave
 2654 number of the N-period optical structure

$$\nu_u = \frac{N\mu_u}{2\pi} = \frac{\text{phase advance over a turn}}{2\pi} \quad (9.20)$$

2655 so that

$$\bar{\beta}_u = \frac{R}{\nu_u} \quad (9.21)$$

2656 the wavelength of the betatron oscillation around the ring. With $k \ll 1$ and using
 2657 Eq. 9.26,

$$\bar{\beta}_x = \frac{\rho_0(1 + k/2)}{\sqrt{1 - n}}, \quad \bar{\beta}_y = \frac{\rho_0(1 + k/2)}{\sqrt{n}} \quad (9.22)$$

2658 Substituting in Eq. 9.16 yields the approximate solution

$$\begin{cases} u(s) \approx \sqrt{\bar{\beta}_u(s)\varepsilon_u/\pi} \cos\left(\nu_u \frac{s}{R} + \phi\right) \\ u'(s) = -\sqrt{\frac{\varepsilon_u/\pi}{\bar{\beta}_u(s)}} \sin\left(\nu_u \frac{s}{R} + \phi\right) + \alpha_u(s) \cos\left(\nu_u \frac{s}{R} + \phi\right) \end{cases} \quad (9.23)$$

2659 In this approximation, the differential equations of motion (Eq. 9.12) can be expressed
 2660 under the form

$$\frac{d^2x}{ds^2} + \frac{\nu_x^2}{R^2}x = 0, \quad \frac{d^2y}{ds^2} + \frac{\nu_y^2}{R^2}y = 0 \quad (9.24)$$

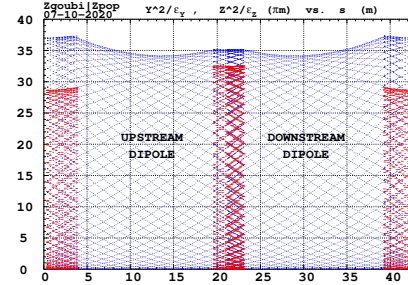
2661 *Beam envelopes*

2662 The beam envelope $\hat{u}(s)$ (with u standing for x or y) is determined by the particle of
 2663 maximum invariant ε_u/π , it is given by

$$\pm \hat{u}(s) = \pm \sqrt{\beta_u(s) \varepsilon_u / \pi} \quad (9.25)$$

As $\beta_u(s)$ is S-periodic, so is the envelope, $\hat{u}(s+S) = \hat{u}(s)$. In a cell with symmetries,

Fig. 9.10 Excursion of a particle along a 43 m long cell, over many turns. The extrema of this motion tangent the envelopes, respectively $\pm (\beta_x(s) \varepsilon_x / \pi)^{1/2}$, horizontal (red), and $\pm (\beta_y(s) \varepsilon_y / \pi)^{1/2}$, vertical (blue), at all s . Envelopes are symmetric with respect to $s = 21.5$ m, a consequence of that very symmetry of the cell



2664 beam envelopes feature the same symmetries, as in Fig. 9.10 for instance: a symmetry
 2665 with respect to the center of the cell; envelop extrema are at azimuth s of $\beta_u(s)$
 2666 extrema, where $\alpha_u = 0$ as $\beta'_u = -2\alpha_u$.
 2667

2668 *Working point*

2669 The “working point” of the synchrotron is the wave number couple (ν_x, ν_y) at which
 2670 the accelerator is operated, it fully characterizes the focusing. In a structure with
 2671 cylindrical symmetry $\nu_x = \sqrt{1-n}$ and $\nu_y = \sqrt{n}$ (Eq. 4.16) so that $\nu_x^2 + \nu_y^2 = 1$: when
 2672 the radial field index n is changed the working point stays on a circle of radius 1 in
 2673 the stability diagram (or “tune diagram”, Fig. 9.11). If drift spaces are added, from
 2674 the linear approximation (Eqs. 9.11, 9.12) it comes

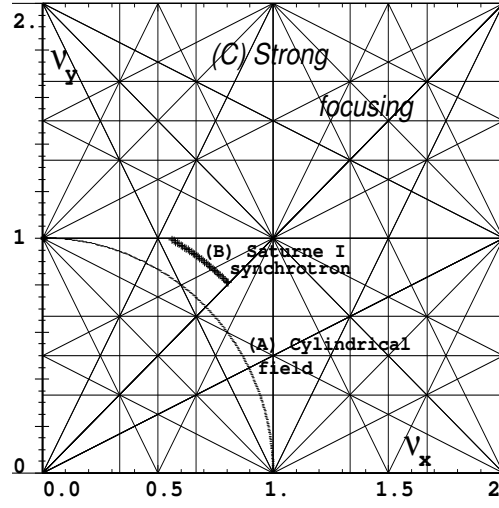
$$\nu_x = \sqrt{(1-n) \frac{R}{\rho_0}}, \quad \nu_y = \sqrt{n \frac{R}{\rho_0}}, \quad \nu_x^2 + \nu_y^2 = \frac{R}{\rho_0} \quad (9.26)$$

thus the working point is located on the circle of radius $\sqrt{R/\rho_0} > 1$. Tunes can not exceed the limits

$$0 < \nu_{x,y} < \sqrt{R/\rho_0}$$

2675 Horizontal and vertical focusing are not independent (Eq. 9.12): if ν_x increases then
 2676 ν_y decreases and reciprocally. This is a lack of flexibility which the advent of strong

Fig. 9.11 Location of the working point in the tune diagram, in case of (A) field with revolution symmetry, on a circle of radius 1; (B) sector field with index + drift spaces, on a circle of radius $(\sqrt{R/\rho_0})$. Case (C) is for strong focusing, ($|n| \gg 1$), ν_x and ν_y are large



2677 focusing will overcome by providing two knobs allowing separate adjustment of the
2678 tunes.

2679 Off-momentum orbits; periodic dispersion

In a dipole with field index $n = -\frac{\rho_0}{B_0} \frac{\partial B_y}{\partial x}$, orbits different momenta $p = p_0 + \Delta p$ are concentric (Fig. 9.8), distant (after Eq. 4.18)

$$\Delta x = \frac{\rho_0}{1-n} \frac{\Delta p}{p_0}$$

2680 from the reference orbit. Introduce now the geometrical radius $R = (1+k)\rho_0$ (Eq. 9.7)
2681 to account for the added drifts, this gives

$$\frac{\Delta x}{\Delta p/p_0} \equiv \frac{\Delta R}{\Delta p/p_0} = \frac{R}{(1-n)(1+k)} \quad (9.27)$$

2682 Thus the chromatic dispersion of the orbits, the dispersion function

$$D = \frac{\Delta x}{\Delta p/p_0} = \frac{R}{(1-n)(1+k)} = \frac{\rho_0}{1-n}, \quad \text{constant} \quad (9.28)$$

2683 an s -independent quantity: in a structure with axial symmetry, comprising drift
2684 sections (Fig. 9.5) or not (classical and AVF cyclotrons for instance), the ratio
2685 $\frac{\Delta x}{\rho_0 \Delta p/p_0}$ is independent of the azimuth s , the distance of a chromatic orbit to the
2686 reference orbit is constant around the ring.

2687 Given that $n < 1$,

- 2688 - higher momentum orbits, $p > p_0$, have a greater radius,
 2689 - lower momentum orbits, $p < p_0$, have a smaller radius.

2690 *Chromatic orbit length*

2691 In an axially symmetric structure the difference in closed orbit length $\Delta C = 2\pi\Delta R$
 2692 resulting from the difference in momentum arises in the dipoles, as all orbits are
 2693 parallel in the drifts (Fig. 9.5). Hence, from Eq. 9.27, the relative closed orbit
 2694 lengthening factor, or momentum compaction

$$\alpha = \frac{\Delta C}{C} \bigg/ \frac{\Delta p}{p_0} \equiv \frac{\Delta R}{R} \bigg/ \frac{\Delta p}{p_0} = \frac{1}{(1-n)(1+k)} \approx \frac{1}{v_x^2} \quad (9.29)$$

2695 with $k = Nl/\pi\rho_0$ (Eq. 9.7). Note that the relationship $\alpha \approx 1/v_x^2$ between momentum
 2696 compaction and horizontal wave number established for a revolution symmetry
 2697 structure (Eq. 4.20) still holds when adding drifts.

2698 **9.1.1.4 Longitudinal Motion**

2699 In a synchrotron, the field B is varied during acceleration (a function performed
 2700 by the power supply) concurrently with the variation of the bunch momentum p (a
 2701 function performed by the accelerating cavity) in such a way that at any time

$$\Delta W = F \times 2\pi R = 2\pi q R \rho \dot{B} B(t) \rho = p(t)/q \quad (9.30)$$

so that the beam is maintained on the design orbit. Given the energies involved, the
 magnet supply imposes its law and the cavity follows $B(t)$ (Fig. 9.12), the best it
 can. The accelerating voltage $\hat{V}(t) = \sin \omega_{\text{rf}} t$ is maintained in synchronism with the
 revolution motion, its angular frequency satisfying

$$\omega_{\text{rf}} = h\omega_{\text{rev}} = h \frac{c}{R} \frac{B(t)}{\sqrt{\left(\frac{m_0}{q\rho}\right)^2 + B^2(t)}}$$

2702 *Energy gain*

2703 The variation of the particle energy over a turn amounts to the work of the force
 2704 $F = dp/dt$ on the charge at the cavity, namely

$$\Delta W = F \times 2\pi R = 2\pi q R \rho \dot{B} \quad (9.31)$$

Over most of the acceleration cycle in a slow-cycling synchrotron \dot{B} is usually
 constant (Eq. 9.3), thus so is ΔW . At Saturne I for instance (the object of Exercise 9.1,

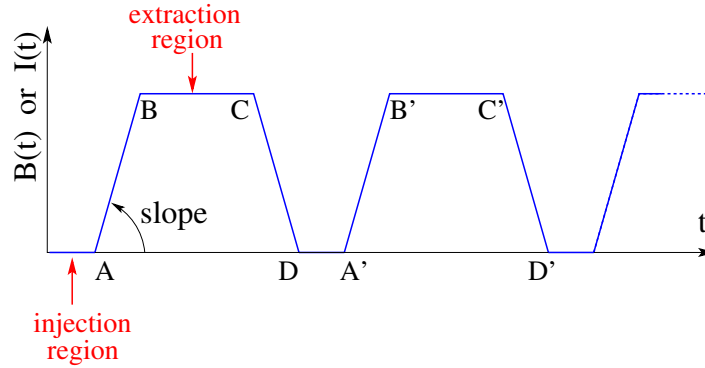


Fig. 9.12 Cycling $B(t)$ in a pulsed synchrotron. Ignoring saturation, $B(t)$ is proportional to the magnet power supply current $I(t)$. Beam injection occurs at low field, in the region of A, extraction occurs at top energy, on the high field plateau. (AB): field ramp up (acceleration); (BC): flat top; (CD): field ramp down; (DA'): thermal relaxation. (AA'): repetition period; $(1/AA')$: repetition rate; *slope*: ramp velocity $\dot{B} = dB/dt$ (Tesla/s).

parameters in Tab. 9.1)

$$\frac{\Delta W}{q} = 2\pi R\rho\dot{B} = 68.9 \times 8.42 \times 1.8 = 1044 \text{ volts}$$

The field ramp lasts

$$\Delta t = (B_{\max} - B_{\min})/\dot{B} \approx B_{\max}/\dot{B} = 0.8 \text{ s}$$

The number of turns to the top energy ($W_{\max} \approx 3 \text{ GeV}$) is

$$N = \frac{W_{\max}}{\Delta W} = \frac{3 \cdot 10^9 \text{ eV}}{1044 \text{ eV/turn}} \approx 3 \cdot 10^6 \text{ turns}$$

The dependence of particle mass on field writes

$$m(t) = \gamma(t)m_0 = \frac{q\rho}{c} \sqrt{\left(\frac{m_0}{qc\rho}\right)^2 + B(t)^2}$$

2705 *Adiabatic damping of the betatron oscillations*

The focusing index (Eq. 9.5) does not change during acceleration, thus the tunes ν_x and ν_y do not change either. As a result of the longitudinal acceleration at the cavity though, the longitudinal energy of the particles is modified. This results in a decrease of the amplitude of betatron oscillations (an increase if the cavity is decelerating). The mechanism is sketched in Fig. 9.13: the slope, respectively before and after (index 2) the cavity is

$$\frac{dx}{ds} = \frac{m \frac{dx}{dt}}{m \frac{ds}{dt}} = \frac{p_x}{p_s}, \quad \frac{dx}{ds} \Big|_2 = \frac{m \frac{dx}{dt} \Big|_2}{m \frac{ds}{dt} \Big|_2} = \frac{p_{x,2}}{p_{s,2}}$$

Particle mass and velocity are modified at the traversal of the cavity but, as the

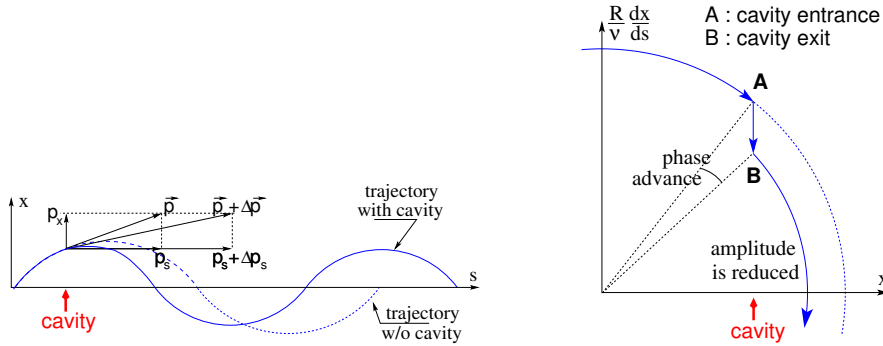


Fig. 9.13 Adiabatic damping of betatron oscillations, here from $x' = p_x/p_s$ before the cavity, to $x'_2 = p_x/(p_s + \Delta p_s)$ after the cavity. In the horizontal phase space, to the right, decrease of $\Delta \left(\frac{dx}{ds} \right)$ if $\frac{dx}{ds} > 0$, increase of $\Delta \left(\frac{dx}{ds} \right)$ if $\frac{dx}{ds} < 0$

force is longitudinal, $dp_x/dt = 0$ thus $p'_x = p_x$, the increase in momentum is purely longitudinal, $p'_s = p_s + \Delta p$. Thus

$$\frac{dx}{ds} \Big|_2 = \frac{p_x}{p_s + \Delta p} \approx \frac{p_x}{p_s} \left(1 - \frac{\Delta p}{p_s} \right)$$

and as a consequence the slope dx/ds varies across the cavity,

$$\Delta \left(\frac{dx}{ds} \right) = \frac{dx}{ds} \Big|_2 - \frac{dx}{ds} = - \frac{dx}{ds} \frac{\Delta p_s}{p_s}$$

2706 The variation of the slope is proportional to the slope, with opposite sign if $\Delta p/p > 0$
 2707 (acceleration) thus a decrease of the slope. This variation has two consequences on
 2708 the betatron oscillation (Fig. 9.13):

- 2709 - a change of the betatron phase,
- 2710 - a modification of the betatron amplitude.

2711 *Coordinate transport*

2712 at the cavity writes $\begin{cases} x_2 = x \\ x'_2 \approx \frac{p_x}{p_s}(1 - \frac{dp}{p}) = x'(1 - \frac{dp}{p}) \end{cases}$. In matrix form, $\begin{pmatrix} x_2 \\ x'_2 \end{pmatrix} =$
 2713 $[C] \begin{pmatrix} x \\ x' \end{pmatrix}$ with

$$[C] = \begin{bmatrix} 1 & 0 \\ 0 & 1 - \frac{dp}{p} \end{bmatrix} \quad (9.32)$$

2714 and $\det[C] = 1 - \frac{dp}{p} \neq 1$: the system is non-conservative, the surface of the beam
 2715 ellipse in phase space is not conserved. Assume one cavity in the ring and note
 2716 $[T] \times [C]$ the one-turn coordinate transport matrix with origin at entrance of the
 2717 cavity. Its determinant is $\det[T] \times \det[C] = \det[C] = 1 - \frac{dp}{p}$; the variation of
 2718 the transverse ellipse surface satisfies $\varepsilon_u = (1 - \frac{dp}{p_0})\varepsilon_0$ or, with $d\varepsilon_u = \varepsilon_u - \varepsilon_0$,
 2719 $\frac{d\varepsilon_u}{\varepsilon_u} = -\frac{dp}{p_0}$, the solution of which is

$$p \varepsilon_u = \text{constant}, \quad \text{or} \quad \beta\gamma\varepsilon_u = \text{constant} \quad (9.33)$$

2720 Over N turns the coordinate transport matrix is $[T_N] = ([T][C])^N$, its determinant
 2721 is $(1 - \frac{dp}{p})^N \approx 1 - N\frac{dp}{p}$: the ellipse surface changes by that factor.

2722 *Synchrotron motion; phase stability*

2723 “Synchrotron motion” designates the mechanism of phase stability, or longitudinal
 2724 focusing (Fig. 9.14), that stabilizes the longitudinal motion of a particle in the vicinity
 2725 of a synchronous phase, ϕ_s , in virtue of

2726 (i) the presence of an accelerating cavity with its frequency indexed on the
 2727 revolution time,

2728 (ii) with the bunch centroid positioned either on the rising slope of the oscillating
 2729 voltage (low energy regime), or on the falling slope (high energy regime).

The synchronous (or “ideal”) particle follows the equilibrium trajectory around
 the ring (the reference closed orbit, about which all other particles will undergo a
 betatron oscillation), its velocity satisfies $v(t) = \frac{qB\rho(t)}{m}$; at each turn it reaches the
 accelerating gap when the oscillating voltage is at the synchronous phase ϕ_s , and
 undergoes an energy gain

$$\Delta W = q\hat{V} \sin \phi_s$$

The condition $|\sin \phi_s| < 1$ imposes a lower limit to the cavity voltage for acceleration
 to happen, namely, after Eq. 9.31,

$$\hat{V} > 2\pi R\rho\dot{B}$$

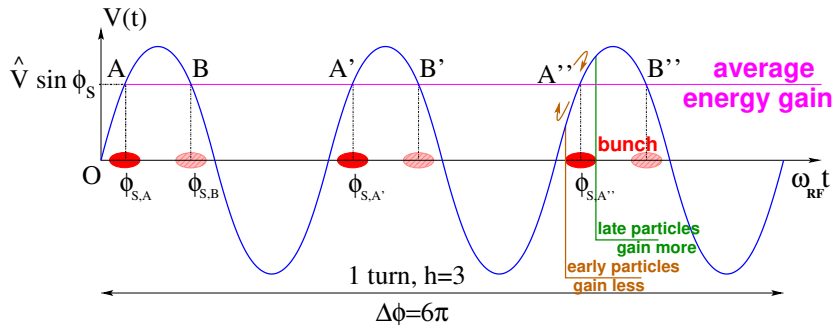


Fig. 9.14 A sketch of the mechanism of phase stability, $h = 3$ in this example. Below transition phase stability occurs for a synchronous phase taken at either one of A, A', A'' arrival times at the gap: a particle with higher energy goes around the ring more rapidly than the synchronous particle; if both are launched together, the former arrives earlier at the voltage gap (at $\phi < \phi_{s,A}$) so experiencing weaker acceleration; at lower energy the particle is slower, it arrives at the gap later, $\phi > \phi_{s,A}$, so experiencing a greater voltage; this results in an overall stable oscillatory motion around the synchronous phase. Beyond transition the stable phase is at either one of B, B', B'' locations: a particle which is less energetic than the synchronous particle arrives earlier, $\phi < \phi_{s,B}$, so experiencing a greater voltage, and inversely, resulting in overall stable synchrotron motion.

2730 Referring to Fig. 9.14, the synchronous phase can be placed on the left (A A' A''...
 2731 series in the Figure, or on the right (B B' B''... series) of the oscillating voltage crest.
 2732 One and only one of these two possibilities, and which one depending upon the optical
 2733 lattice and on particle energy, ensures that particles in a bunch remain grouped in
 2734 the vicinity of the synchronous particle. The transition is between two time-of-flight
 2735 regimes: a particle which gains momentum compared to the synchronous particle
 2736 has a greater velocity, while
 2737 - in the high bunch energy regime the increase in path length around the ring
 2738 is faster than the increase in velocity (velocity essentially does not even change
 2739 in ultrarelativistic regime), a revolution around the ring takes more time (this is the
 2740 classical cyclotron and synchrocyclotron regime, and as well the high energy electron
 2741 synchrotron regime); consider such a particle, arriving at the accelerating gap late
 2742 ($\phi(t) > \phi_s$), in order for it to be pulled toward bunch center (*i.e.*, take less time
 2743 around the ring) it has to undergo deceleration; this is the B series, above transition;
 2744 - in the low bunch energy regime velocity increase is faster than path length
 2745 increase, thus a revolution around the ring is faster; consider such a particle,
 2746 arriving at the accelerating gap early ($\phi(t) < \phi_s$), in order for it to be pulled toward
 2747 bunch center (*i.e.*, take more time around the ring) it has to be slowed down, it has to
 2748 undergo deceleration; this is the A series, below transition.

2749 *Transition energy*

2750 The transition between the two time-of-flight regimes occurs at $\frac{dT_{\text{rev}}}{T_{\text{rev}}} = 0$. With
 2751 $T = 2\pi/\omega = C/v$, this can be written $\frac{d\omega_{\text{rev}}}{\omega_{\text{rev}}} = -\frac{dT_{\text{rev}}}{T_{\text{rev}}} = \frac{dv}{v} - \frac{dC}{C}$. With $\frac{dv}{v} = \frac{1}{\gamma^2} \frac{dp}{p}$
 2752 and momentum compaction $\alpha = \frac{dC}{C} / \frac{dp}{p}$, (Eq. 9.29), this can be written

$$\frac{d\omega_{\text{rev}}}{\omega_{\text{rev}}} = -\frac{dT_{\text{rev}}}{T_{\text{rev}}} = \left(\frac{1}{\gamma^2} - \alpha \right) \frac{dp}{p} = \eta \frac{dp}{p} \quad (9.34)$$

2753 wherein the phase-slip factor has been introduced,

$$\eta = \overbrace{\frac{1}{\gamma^2}}^{\text{kinematics}} - \underbrace{\alpha}_{\text{lattice}} = \frac{1}{\gamma^2} - \frac{1}{\gamma_{\text{tr}}^2} \quad (9.35)$$

2754 The transition γ appears to be a property of the lattice.

2755 In a weak focusing lattice $\gamma_{\text{tr}} = 1/\sqrt{\alpha} \approx \nu_x$ (Eqs. 4.20, 9.29), thus the phase
 2756 stability regime is

$$\begin{aligned} &\text{below transition, i.e. } \phi_s < \pi/2, && \text{if } \gamma < \nu_x \\ &\text{above transition, i.e. } \phi_s > \pi/2, && \text{if } \gamma > \nu_x \end{aligned} \quad (9.36)$$

2757 In a weak focusing synchrotron the horizontal tune $\nu_x = \sqrt{(1-n)R/\rho_0}$ (Eq. 9.26)
 2758 may be $\gtrsim 1$, and subsequently $\gamma_{\text{tr}} > 1$ is a possibility. There is no transition-gamma
 2759 if $\nu_x < 1$. Acceleration to 3 GeV in Saturne I for instance, from 50 MeV at injection,
 2760 and with $\nu_x \approx 0.7$ (Tab. 9.1) did not require transition-gamma crossing³.

2761 **9.1.2 Spin Motion, Depolarizing Resonances**

2762 The field index is essentially zero in the ZGS, transverse focusing is ensured by
 2763 wedge angles at the ends of the height dipoles, which is thus the only location where
 2764 non-zero horizontal field components are found. As a consequence depolarizing
 2765 resonances are weak: “As we can see from the table, the transition probability [from
 2766 spin state $\psi_{1/2}$ to spin state $\psi_{-1/2}$] is reasonably small up to $\gamma = 7.1$ ” [13], i.e.
 2767 $G\gamma = 12.73$, $p = 6.6$ GeV/c; the table referred to stipulates a transition probability
 2768 $P_{\frac{1}{2}, -\frac{1}{2}} < 0.042$, whereas resonances beyond that energy range feature $P_{\frac{1}{2}, -\frac{1}{2}} > 0.36$.

³ Transition-gamma crossing, or “gamma jump”, is a common beam manipulation during acceleration in strong focusing synchrotrons, it requires an RF phase jump, the technique is addressed in Chapter 10.

2769 Beam depolarization up to 6 GeV/c, under the effect of these resonances, is illustrated
 2770 in Fig. 9.15.

2771 In a synchrotron using gradient dipoles, particles experience radial fields all along
 2772 the latter as they undergo vertical betatron oscillations, as an effect of the radial field
 2773 index [13, 20, 21]. However these radial field components are weak, and so is there
 2774 effect on spin motion as long as the particle energy is low enough (an effect of the γ
 2775 factor in the spin precession Eq. 4.28, Chap. 4).

Assuming a defect-free ring, the vertical betatron motion excites “intrinsic” spin resonances, located at

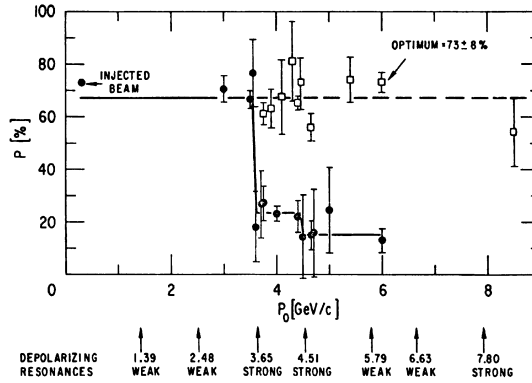
$$G\gamma_R = k P \pm \nu_y$$

with k an integer and P the period of the ring. In the ZGS for instance, $\nu_y \approx 0.8$ (Tab. 9.2), the ring is $P=4$ -periodic, thus $G\gamma_R = 4k \pm 0.8$. Strongest resonances are located at

$$G\gamma_R = mk P \pm \nu_y$$

2776 with m the number of cells per superperiod [22, Sec. 3.II]. In the ZGS, $m=2$ thus
 2777 strongest resonances occur at $G\gamma_R = 2 \times 4k \pm 0.8 = 7.2$ ($p = 3.65$ GeV/c), 8.8 (4.51 GeV/c), 15.2 (7.9 GeV/c), ... (Fig. 9.15).

Fig. 9.15 Depolarizing intrinsic resonance landscape up to 9 GeV/c at the ZGS (solid circles) [23]. Systematic resonances are located at $G\gamma_R = 4 \times \text{integer} \pm \nu_y$, stronger ones at $G\gamma_R = 8 \times \text{integer} \pm \nu_y$. A tune jump was applied to preserve polarization when crossing strong resonances (empty circles)



2778

In the presence of vertical orbit defects, non-zero periodic transverse fields are experienced along the closed orbit, they excite “imperfection” depolarizing resonances, located at

$$G\gamma_R = k$$

with k an integer. In the case of systematic defects the periodicity of the orbit is that of the lattice, P , imperfection resonances are located at $G\gamma_R = kP$. Strongest imperfection resonances are located at [22, Sec. 3.II]

$$G\gamma_R = mk P$$

2779 Crossing a depolarizing resonance of strength ϵ_R causes a loss of polarization
2780 given by (Froissart-Stora formula [24])

$$\frac{P_f}{P_i} = 2e^{-\frac{\pi}{2} \frac{|\epsilon_R|^2}{\alpha}} - 1 \quad (9.37)$$

2781 from a value P_i upstream to an asymptotic value P_f downstream of the resonance.
2782 This assumes an isolated resonance, crossed at an energy gain ΔE per turn, with a
2783 crossing speed

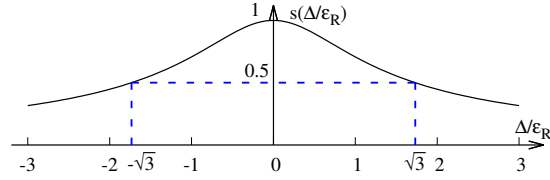
$$\alpha = G \frac{d\gamma}{d\theta} = \frac{1}{2\pi} \frac{\Delta E}{M} \quad (9.38)$$

2784 *Spin precession axis. Resonance width*

2785 Consider the spin vector $\mathbf{S}(\theta) = (S_\eta, S_\xi, S_y)$ of a particle in the laboratory frame,
2786 with θ the orbital angle around the accelerator. Introduce the projection $s(\theta)$ of \mathbf{S}
2787 in the median plane

$$s(\theta) = S_\eta(\theta) + jS_\xi(\theta) \quad (\text{and } S_y^2 = 1 - s^2) \quad (9.39)$$

Fig. 9.16 Modulus of the horizontal spin component. $s = 1/2$ at distance $\Delta = \pm\sqrt{3}\epsilon_R$ from $G\gamma_R$



2788

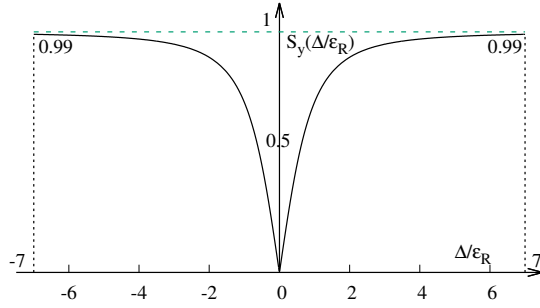
2789 It can be shown that in the case of a stationary solution of the spin motion, viz.
2790 the spin precession axis, s satisfies [21] (Fig. 9.16)

$$s^2 = \frac{1}{1 + \frac{\Delta^2}{|\epsilon_R|^2}} \quad (9.40)$$

2791 with $\Delta = G\gamma - G\gamma_R$ the distance to the resonance. The resonance width is a measure
2792 of its strength (Fig. 9.17). The quantity of interest is the angle, ϕ , of the spin
2793 precession direction to the vertical axis, given by (Fig. 9.17)

$$\cos \phi(\Delta) \equiv S_y(\Delta) = \sqrt{1 - s^2} = \frac{\Delta/|\epsilon_R|}{\sqrt{1 + \Delta^2/|\epsilon_R|^2}} \quad (9.41)$$

Fig. 9.17 Dependence of polarization on the distance to the resonance. For instance $S_y = 0.99$, 1% depolarization, corresponds to $\Delta = 7|\epsilon_R|$. On the resonance, $\Delta = 0$, the precession axis lies in the median plane, $S_y = 0$



2794 On the resonance, $\Delta = 0$, the spin precession axis lies in the bend plane: $\phi = \pm\pi/2$.
 2795 $S_y = 0.99$ (1% depolarization) corresponds to a distance to the resonance $\Delta = 7|\epsilon_R|$,
 2796 spin precession axis at an angle $\phi = \text{acos}(0.99) = 8^\circ$ from the vertical.

2797 Conversely, given S_y ,

$$\frac{\Delta^2}{|\epsilon_R|^2} = \frac{S_y^2}{1 - S_y^2} \tag{9.42}$$

The precession axis is common to all spins, S_y is a measure of the polarization along the vertical axis,

$$S_y = \frac{N^+ - N^-}{N^+ + N^-}$$

2798 wherein N^+ and N^- denote the number of particles in spin states $\frac{1}{2}$ and $-\frac{1}{2}$ respectively.
 2799

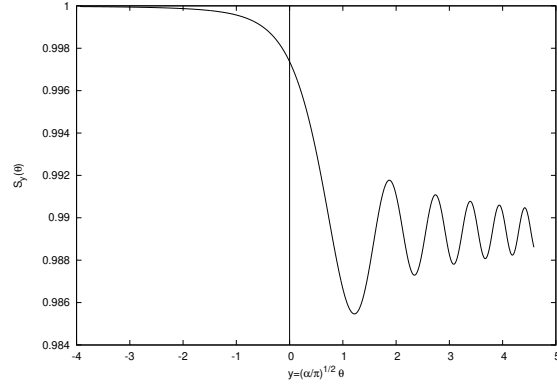
2800 *Spin motion through weak resonances*

Depolarizing resonances are weak up to several GeV in a weak focusing synchrotron, as the radial and/or longitudinal fields, which stem from a small radial field index and from dipole fringe fields, are weak. Spin motion $S_y(\theta)$ through a resonance in that case can be assumed to satisfy $S_{y,f} \approx S_{y,i}$, with $S_{y,f}$ and $S_{y,i}$ the asymptotic vertical spin component values respectively upstream and downstream of the resonance). As a consequence it can be calculated in terms of the Fresnel integrals [20, 21]

$$C(x) = \int_0^x \cos\left(\frac{\pi}{2}t^2\right) dt, \quad S(x) = \int_0^x \sin\left(\frac{\pi}{2}t^2\right) dt$$

2801 namely, with the origin of the orbital angle is taken at the resonance (Fig. 9.18),

Fig. 9.18 Vertical component of spin motion $S_y(\theta)$ through a weak depolarizing resonance (after Eq. 9.43). The vertical bar is at the location of the resonance, which coincides with the origin of the orbital angle



$$\begin{aligned}
 \text{if } \theta < 0 : \left(\frac{S_y(\theta)}{S_{y,i}} \right)^2 &= 1 - \frac{\pi}{\alpha} |\epsilon_R|^2 \left\{ \left[0.5 - C \left(-\theta \sqrt{\frac{\alpha}{\pi}} \right) \right]^2 + \left[0.5 - S \left(-\theta \sqrt{\frac{\alpha}{\pi}} \right) \right]^2 \right\} \\
 \text{if } \theta > 0 : \left(\frac{S_y(\theta)}{S_{y,i}} \right)^2 &= 1 - \frac{\pi}{\alpha} |\epsilon_R|^2 \left\{ \left[0.5 + C \left(\theta \sqrt{\frac{\alpha}{\pi}} \right) \right]^2 + \left[0.5 + S \left(\theta \sqrt{\frac{\alpha}{\pi}} \right) \right]^2 \right\} \quad (9.43)
 \end{aligned}$$

2802 In the asymptotic limit,

$$\frac{S_y(\theta)}{S_{y,i}} \xrightarrow{\theta \rightarrow \infty} 1 - \frac{\pi}{\alpha} |\epsilon_R|^2 \quad (9.44)$$

2803 which identifies with the development of Froissart-Stora formula $P_f/P_i =$

2804 $2 \exp\left(-\frac{\pi}{2} \frac{|\epsilon_R|^2}{\alpha}\right) - 1$ to the first order in $|\epsilon_R|^2/\alpha$. This approximation holds in the limit
 2805 that higher order terms can be neglected: $|\epsilon_R|^2/\alpha \ll 1$.

2806 9.2 Exercises

2807 9.1 Construct Saturne I (weak index) synchrotron. Spin Resonances

2808 Solution: page 344

2809 In this exercise, Saturne I weak focusing 3 GeV synchrotron is modeled. Spin
 2810 resonances in a weak dipole gradient lattice are studied.

2811 (a) Construct a model of Saturne I 90° cell dipole in the hard-edge model, using
 2812 DIPOLE. Use the parameters given in Tab. 9.1, and Fig. 9.19 as a guidance. In order
 2813 to allow beam monitoring, split the dipole in two 45° deg halves. It is judicious to
 2814 take $RM=841.93$ cm in DIPOLE, as this is the reference radius for the definition of
 2815 the radial index. Take an integration step size in centimeter range - small enough to
 2816 ensure numerical convergence, as large as doable for fast multiturn raytracing.

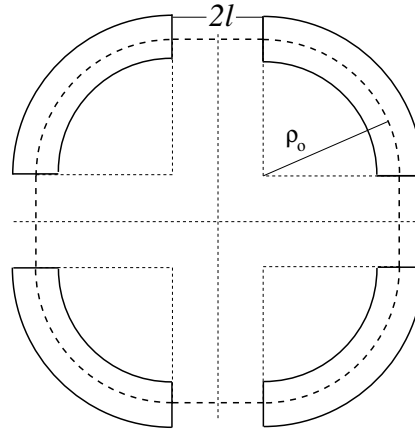


Fig. 9.19 A schematic layout of Saturne I, a $2\pi/4$ axial symmetry structure, comprised of 4 radial field index 90 deg dipoles and 4 drift spaces. The cell in the simulation exercises is taken as a $\pi/4$ quadrant: l-drift/90°-dipole/l-drift

Table 9.1 Parameters of Saturne 1 weak focusing synchrotron [25]. ρ_0 denotes the reference bending radius in the dipole; the reference orbit, field index, wave numbers, etc., are taken along that radius

| | | |
|---------------------------------|----------|------------------------------------|
| Orbit length, C | cm | 6890 |
| Average radius, $R = C/2\pi$ | cm | 1096.58 |
| Straight section length, $2l$ | cm | 400 |
| Magnetic radius, ρ_0 | cm | 841.93 |
| R/ρ_0 | | 1.30246 |
| Field index n , nominal value | | 0.6 |
| Wave numbers, $\nu_x; \nu_y$ | | 0.724; 0.889 **** verif wrt. simul |
| Stability limit | | $0.5 < n < 0.757$ |
| Injection energy | MeV | 3.6 |
| Field at injection | kG | 0.0326 |
| Top energy | GeV | 2.94 |
| \dot{B} | T/s | 1.8 |
| Field at top energy, B_{\max} | kG | 14.9 |
| $B_{\max}\rho$ | T m | 13 |
| Field ramp at injection | kG/s | 20 |
| Synchronous energy gain | keV/turn | 1.160 |
| RF harmonic | | 2 |

2817 Validate the model by producing the 6×6 transport matrix of the cell dipole
 2818 (MATRIX[IFOC=0] can be used for that, with OBJET[KOBJ=5] to define a proper
 2819 set of paraxial initial coordinates) and checking against theory (Sect. 18.2, Eq. 18.6).

2820 (b) Construct a model of Saturne I cell, with origin at the center of the drift.
 2821 Find the closed orbit, that particular trajectory which has all its coordinates zero in
 2822 the drifts: use DIPOLE[KPOS] to cancel the closed orbit coordinates at DIPOLE
 2823 ends. While there, check the expected value of the dispersion (Eq. 9.28) and of
 2824 the momentum compaction (Eq. 9.29), from the raytracing of a chromatic closed
 2825 orbit - *i.e.*, the orbit of an off-momentum particle. Plot these two orbits (on- and
 2826 off-momentum), over a complete turn around the ring, on a common graph.

2827 Compute the cell periodic optical functions and tunes, using either MA-
 2828 TRIX[IFOC=11] or TWISS; check their values against theory. Check consistency
 2829 with previous dispersion function and momentum compaction outcomes.

2830 Move the origin of the lattice at a different azimuth s along the cell: verify that,
 2831 while the transport matrix depends on the origin, its trace does not.

2832 Produce a graph of the optical functions (betatron functions and dispersion) along
 2833 the cell. Check the expected average values of the betatron functions (Eq. 9.22).

2834 Produce a scan of the tunes over the field index range $0.5 \leq n \leq 0.757$. RE-
 2835 BELOTE can be used to repeatedly change n over that range. Superimpose the
 2836 theoretical curves $\nu_x(n)$, $\nu_y(n)$.

2837 (c) Launch 60 particles evenly distributed on a common paraxial horizontal
 2838 Courant-Snyder invariant (vertical motion is taken null). Store particle data along
 2839 the ring in zgoubi.plt, using DIPOLE[IL=2] and DRIFT[split,N=20,IL=2]. Use these
 2840 to generate a graph of the beam envelopes.

2841 Using Eq. 9.25 compare with the results obtained in (b). Find the minimum
 2842 and maximum values of the betatron functions, and their azimuth $s(\min[\beta_x])$,
 2843 $s(\max[\beta_x])$. Check the latter against theory.

2844 Repeat for the vertical motion, taking $\varepsilon_x = 0$, ε_y paraxial.

2845 Repeat, using, instead of 60 particles, a single particle traced over a few tens of
 2846 turns.

2847 (d) Produce an acceleration cycle from 3.6 MeV to 3 GeV, for a few particles
 2848 launched on a common $10^{-4} \pi\text{m}$ initial invariant in each plane. Ignore synchrotron
 2849 motion (CAVITE[IOPT=3] can be used in that case). Take a peak voltage $\hat{V} = 200 \text{ kV}$
 2850 (unrealistic though, as it would result in a nonphysical \hat{B} (Eq. 9.31)) and synchronous
 2851 phase $\phi_s = 150 \text{ deg}$ (justify $\phi_s > \pi/2$).

2852 Check the betatron damping over the acceleration range: compare with theory
 2853 (Eq. 9.33).

2854 How close to symplectic the numerical integration is (it is by definition *not*
 2855 symplectic, being a truncated Taylor series method [26, Eq. 1.2.4]), depends on the
 2856 integration step size, and on the size of the flying mesh in the DIPOLE method [26,
 2857 Fig. 20]; check a possible departure of the betatron damping from theory as a function
 2858 of these parameters.

2859 Produce a graph of the horizontal and vertical wave number values over the
 2860 acceleration cycle.

2861 (e) Some spin motion, now. Adding SPNTRK at the beginning of the sequence
 2862 will ensure spin tracking.

2863 Based on the file worked out for question (d), simulate the acceleration of a single
 2864 particle, through the intrinsic resonance $G\gamma_R = 4 - \nu_Z$, from a few thousand turns
 2865 upstream to a few thousand turns downstream. On a common graph, plot $S_y(\text{turn})$
 2866 for a few different values of the vertical betatron invariant (the horizontal invariant
 2867 value does not matter - explain that statement, it can be taken zero).

2868 (f) Produce a graph of the average value of S_Z over a 200 particle set, as a function
 2869 of $G\gamma$, across the $G\gamma_R = 4 - \nu_Z$ resonance. Indicate on that graph the location of
 2870 the resonant $G\gamma_R$ values.

2871 Perform this resonance crossing for five different values of the particle invariant:
 2872 $\varepsilon_Z/\pi = 2, 10, 20, 40, 200 \mu\text{m}$. Compute P_f/P_i in each case, check the dependence
 2873 on ε_Z against theory.

2874 Compute the resonance strength, ε_Z , from these trackings.

2875 Re-do this crossing simulation for a different crossing speed (take for instance
 2876 $\hat{V} = 10 \text{ kV}$) and a couple of vertical invariant values, compute P_f/P_i so obtained.
 2877 Check the crossing speed dependence of P_f/P_i against theory.

2878 (g) Show that the previous weak resonance crossings ($P_f/P_i \approx 1$) satisfies
 2879 Eq. 9.43. Match the tracking data to the latter to get the vertical betatron tune
 2880 ν_y , the location of the resonance $G\gamma_R$, and its strength.

2881 (h) Track a few particles at fixed energy, at distances from the resonance $G\gamma_R =$
 2882 $4 - \nu_y$ of up to a $7 \times \varepsilon_R$ (this distance corresponds to 1% depolarization).

2883 Produce on a common graph the spin motion $S_Z(\text{turn})$ for all these particles, as
 2884 observed at some azimuth along the ring.

2885 Produce a graph of $\langle S_y \rangle|_{\text{turn}}(\Delta)$ (as in Fig. 9.17).

Produce the vertical betatron tune ν_y , the location of the resonance $G\gamma_R$, and its
 strength, obtained from a match of these tracking trials to (Eq. 9.41)

$$\langle S_y \rangle (\Delta) = \frac{\Delta}{\sqrt{|\varepsilon_R|^2 + \Delta^2}}$$

2886 9.2 Construct the ZGS (zero-gradient) synchrotron. Spin Resonances

2887 Solution: page 369

2888 In this exercise, the ZGS 12 GeV synchrotron is modeled in `zgoubi`. Spin reso-
 2889 nances in ZGS wedge focusing zero-gradient synchrotron are studied.

2890 (a) Construct a model of ZGS 45° cell dipole in the hard-edge model, using
 2891 DIPOLE. Use the parameters given in Tab. 9.2, and Figs. 9.20, 9.21 as a guidance.
 2892 In order to allow beam monitoring, split the dipole in two 22.5° deg halves. Take the
 2893 closed orbit radius as the reference $RM=2076 \text{ cm}$ in DIPOLE: it will be assumed
 2894 that the orbit is the same at all energies⁴. Take an integration step size in centimeter
 2895 range - small enough to ensure numerical convergence, as large as doable for fast
 2896 multiturn raytracing.

2897 Validate the model by producing the 6×6 transport matrices of both dipole
 2898 (MATRIX[IFOC=0] can be used for that, with OBJET[KOBJ=5] to define a proper
 2899 set of paraxial initial coordinates) and checking against theory (Sect. 18.2, Eq. 18.6).

2900 Add fringe fields in DIPOLE[$\lambda, C_0 - C_5$], the rest if the exercise will use that
 2901 model. Take fringe field extent and coefficient values

$$\lambda = 60 \text{ cm } C_0 = 0.1455, C_1 = 2.2670, C_2 = -0.6395, C_3 = 1.1558, C_4 = C_5 = 0 \quad (9.45)$$

2902 ($C_0 - C_5$ determine the shape of the field fall-off, they have been computed from a
 2903 typical measured field profile $B(s)$).

⁴ Note that in reality the reference orbit in ZGS moved outward during acceleration [27].

2904 (b) Construct a model of ZGS cell accounting for dipole fringe fields, with origin
 2905 at the center of the long drift. In doing so, use `DIPOLE[KPOS]` to cancel the closed
 2906 orbit coordinates at `DIPOLE` ends.

2907 Compute the periodic optical functions at cell ends, and cell tunes, using `MA-`
 2908 `TRIX[IFOC=11]`; check their values against theory.

2909 Move the origin at the location (azimuth s along the cell) of the betatron functions
 2910 extrema: verify that, while the transport matrix depends on the origin, its trace does
 2911 not. Verify that the local betatron function extrema, and the dispersion function, have
 2912 the expected values.

2913 Produce a graph of the optical functions (betatron functions and dispersion) along
 2914 the cell.

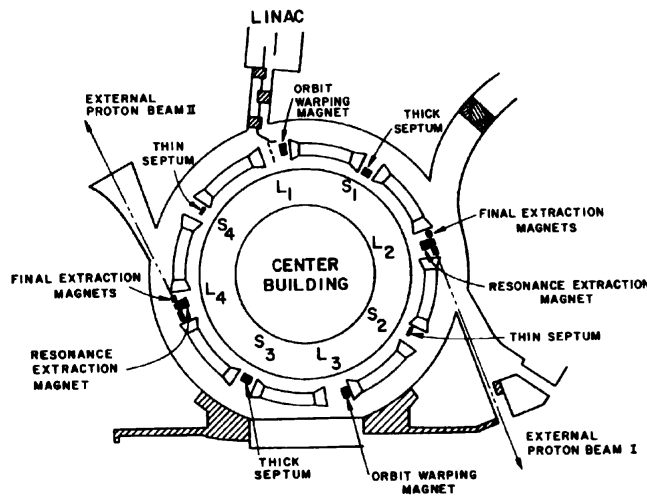


Fig. 9.20 A schematic layout of the ZGS [23], a $\pi/2$ -periodic structure, comprised of 8 zero-index dipoles, 4 long and 4 short straight sections

2915 (c) Additional verifications regarding the model.

2916 Produce a graph of the field $B(s)$

2917 - along the on-momentum closed orbit, and along off-momentum chromatic closed
 2918 orbits, across a cell;

2919 - along orbits at large horizontal excursion;

2920 - along orbits at large vertical excursion.

2921 For all these cases, verify qualitatively, from the graphs, that $B(s)$ appears as
 2922 expected.

(d) Justify considering the betatron oscillation as sinusoidal, namely,

$$y(\theta) = A \cos(\nu_y \theta + \phi)$$

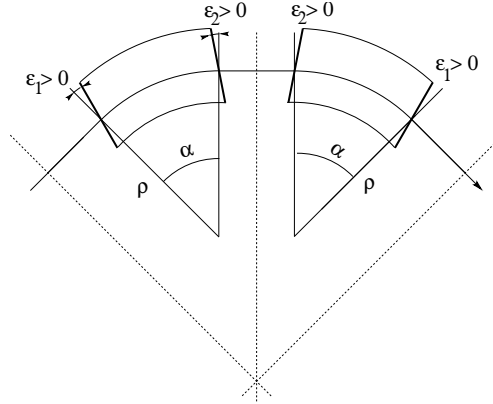


Fig. 9.21 A sketch of ZGS cell layout. In defining the entrance and exit faces (EFBs) of the magnet, beam goes from left to right. Wedge angles at the long straight sections (ε_1) and at the short straight sections (ε_2) are different

Table 9.2 Parameters of the ZGS weak focusing synchrotron after Refs. [27, 28] [23, pp. 288-294, p. 716] (2nd column, when they are known) and in the present simplified model and numerical simulations (3rd column). Note that the actual orbit moves during ZGS acceleration cycle, tunes change as well - this is not taken into account in the present modeling, for simplicity

| | | From Refs. [27, 28] | Simplified model |
|---|-------------------|------------------------|--|
| Injection energy | MeV | | 50 |
| Top energy | GeV | | 12.5 |
| $G\gamma$ span | | | 1.888387 - 25.67781 |
| Length of central orbit | m | 171.8 | 170.90457 |
| Length of straight sections, total | m | 41.45 | 40.44 |
| <i>Lattice</i> | | | |
| Wave numbers $\nu_x; \nu_y$ | | 0.82; 0.79 | 0.849; 0.771 |
| Max. $\beta_x; \beta_y$ | m | | 32.5; 37.1 |
| <i>Magnet</i> | | | |
| Length | m | 16.3 | 16.30486 (magnetic) |
| Magnetic radius | m | 21.716 | 20.76 |
| Field min.; max. | kG | 0.482; 21.5 | 0.4986; 21.54 |
| Field index | | | 0 |
| Yoke angular extent | deg | 43.02590 | 45 |
| Wedge angle | deg | ≈ 10 | 13 and 8 |
| <i>RF</i> | | | |
| Rev. frequency | MHz | 0.55 - 1.75 | 0.551 - 1.751 |
| RF harmonic $h = \omega_{rf} / \omega_{rev}$ | | | 8 |
| Peak voltage | kV | 20 | 200 |
| B-dot, nominal/max. | T/s | 2.15/2.6 | |
| Energy gain, nominal/max. | keV/turn | 8.3/10 | 100 |
| Synchronous phase, nominal | deg | | 150 |
| <i>Beam</i> | | | |
| $\varepsilon_x; \varepsilon_y$ (at injection) | $\pi \mu\text{m}$ | | 25; 150 |
| Momentum spread, rms | | | 3×10^{-4} |
| Polarization at injection | % | > 75 | 100 |
| Radial width of beam (90%), at inj. | inch | 2.5 | $\sqrt{\beta_x \varepsilon_x / \pi} = 1.1$ |

2923 wherein $\theta = s/R$, $R = \oint ds/2\pi$.

2924 Find the value of the horizontal and vertical betatron functions, resulting from
2925 that approximation. Compare with the betatron functions obtained in (b).

2926 (e) Produce an acceleration cycle from 50 MeV to 17 GeV about, for a few particles
2927 launched on a common $10^{-5} \pi m$ vertical initial invariant, with small horizontal
2928 invariant. Ignore synchrotron motion (CAVITE[IOPT=3] can be used in that case).
2929 Take a peak voltage $\hat{V} = 200$ kV (this is unrealistic but yields 10 times faster
2930 computing than the actual $\hat{V} = 20$ kV, Tab. 9.2) and synchronous phase $\phi_s = 150$ deg
2931 (justify $\phi_s > \pi/2$). Add spin, using SPNTRK, in view of the next question, (f).

2932 Check the accuracy of the betatron damping over the acceleration range, compared
2933 to theory. How close to symplectic the numerical integration is (it is by definition
2934 *not* symplectic), depends on the integration step size, and on the size of the flying
2935 mesh in the DIPOLE method [26, Fig. 20]; check a possible departure of the betatron
2936 damping from theory as a function of these parameters.

2937 Produce a graph of the evolution of the horizontal and vertical wave numbers
2938 during the acceleration cycle.

2939 (f) Using the raytracing material developed in (e): produce a graph of the vertical
2940 spin component of the particles, and the average value over that 200 particle set, as
2941 a function of $G\gamma$. Indicate on that graph the location of the resonant $G\gamma_R$ values.

2942 (g) Based on the simulation file used in (f), simulate the acceleration of a single
 2943 particle, through one particular intrinsic resonance, from a few thousand turns
 2944 upstream to a few thousand turns downstream.

2945 Perform this resonance crossing for different values of the particle invariant.
 2946 Determine the dependence of final/initial vertical spin component value, on the
 2947 invariant value; check against theory.

2948 Re-do this crossing simulation for a different crossing speed. Check the crossing
 2949 speed dependence of final/initial vertical spin component so obtained, against theory.

2950 (h) Introduce a vertical orbit defect in the ZGS ring.

2951 Find the closed orbit.

2952 Accelerate a particle launched on that closed orbit, from 50 MeV to 17 GeV about,
 2953 produce a graph of the vertical spin component.

2954 Select one particular resonance, reproduce the two methods of (g) to check the
 2955 location of the resonance at $G\gamma_R = \text{integer}$, and to find its strength.

2956 References

- 2957 1. Veksler, V.: A new method of acceleration of relativistic particles. J. of Phys. USSR 9 153-158
 2958 (1945)
- 2959 2. McMillan, E. M.: The Synchrotron. Phys. Rev. 68 143-144 (1945)
- 2960 3. Goward, F. K., and Barnes, D. E.: Experimental 8 MeV synchrotron for electron acceleration.
 2961 Nature 158, 413 (1946)
- 2962 4. Richardson, J.R., et al.: Frequency Modulated Cyclotron. Phys. Rev. 69: 669 (1946)
- 2963 5. Kerst, D. W.: The Acceleration of Electrons by Magnetic Induction.. Phys. Rev., 60, 47-53
 2964 (1941)
- 2965 6. Photo saturne I. ***** TB completed **** Archives historiques CEA. Copyright
 2966 CEA/Service de documentation - FAR_SA_N_00248
- 2967 7. Photo tranche dipole. Credit: CEA Saclay. ***** TB completed *****
 2968 Archives historiques CEA. Copyright CEA/Service de documentation - FAR_SA_N_02826
- 2969 8. Sessler, A., Wilson, E.: Engines of Discovery. A Century of Particle Accelerators. World
 2970 Scientific, 2007
- 2971 9. ***** fnal loma linda synch copyrights *****
- 2972 10. Endo, K., et al.: Compact proton and carbon ion synchrotrons for radiation therapy. MOPRI087,
 2973 Proceedings of EPAC 2002, Paris, France; pp. 2733-2735.
 2974 <https://accelconf.web.cern.ch/e02/PAPERS/MOPRI087.pdf>
- 2975 11. Vostrikov, V.A., et al.: Novel approach to design of the compact proton synchrotron magnetic
 2976 lattice. tupsa17, 26th Russian Particle Accelerator Conference RUPAC2018, Protvino, Russia
 2977 (2018).
 2978 <https://accelconf.web.cern.ch/rupac2018/papers/tupsa17.pdf>
- 2979 12. Cohen, D., : Feasibility of Accelerating Polarized Protons with the Argonne ZGS. Review of
 2980 Scientific Instruments 33, 161 (1962).// <https://doi.org/10.1063/1.1746524>
- 2981 13. Ratner, L.G. and Khoe, T.K.: Acceleration of Polarized Protons in the Zero Gradient Syn-
 2982 chrotron. Procs. PAC 1973 Conference, Washington (1973).
 2983 http://accelconf.web.cern.ch/p73/PDF/PAC1973_0217.PDF
- 2984 14. Cho, Y., et als.: Effects of depolarizing resonances on a circulating beam of polarized protons
 2985 during or storage in a synchrotron. IEEE Trans. Nuclear Science, Vol.NS-24, No.3, June 1977

- 2986 15. Parker, E.F.: High Energy Polarized Deuterons at the Argonne National Laboratory Zero
2987 Gradient Synchrotron. IEEE Transactions on Nuclear Science, Vol. NS-26, No. 3, June 1979,
2988 pp 3200-3202
- 2989 16. Leleux, G.: Accélérateurs Circulaires. Lecture Notes, INSTN, CEA Saclay (1978)
- 2990 17. Suddeth, D.E., et als.: Pole face winding equipment for eddy current correction at the Zero
2991 Gradient Synchrotron. Procs. PAC 1973 Conference, Washington (1973).
2992 http://accelconf.web.cern.ch/p73/PDF/PAC1973_0397.PDF
- 2993 18. Rauchas, A.V. and Wright, A.J.: Betatron tune profile control in the Zero Gradient Synchrotron
2994 (ZGS) using the main magnet pole face windings. Procs. PAC1977 conference, IEEE Trans.
2995 on Nucl. Science, VoL.NS-24, No.3, June 1977
- 2996 19. Floquet, G.: Sur les équations différentielles linéaires à coefficients périodiques. Annales
2997 scientifiques de l'E.N.S. 2e série, tome 12 (1883), p. 47-88.
2998 http://www.numdam.org/item?id=ASENS_1883_2_12_47_0
- 2999 20. Leleux, G.: Traversée des résonances de dépolarisation. Rapport Interne LNS/GT-91-15,
3000 Saturne, Groupe Théorie, CEA Saclay (février 1991)
- 3001 21. Méot, F.: Spin Dynamics. Polarized Beam Dynamics and Instrumentation in Particle Accel-
3002 erators: USPAS Summer 2021 Spin Class Lectures, Springer (2023)
- 3003 22. Lee, S.Y.: Spin Dynamics and Snakes in Synchrotrons. World Scientific, 1997
- 3004 23. Khoe, T.K., et al.: The High Energy Polarized Beam at the ZGS. Procs. IXth Int. Conf on
3005 High Energy Accelerators, Dubna, pp. 288-294 (1974).
- 3006 24. Froissart, M. and Stora, R.: Dépolarisation d'un faisceau de protons polarisés dans un syn-
3007 chrotron. Nucl. Inst. Meth. 7 (1960) 297.
- 3008 25. Bruck H., Debraine P., Levy-Mandel R., Lutz J., Podliasky I., Prevot F., Taieb J., Winter S.D.,
3009 Maillet R., Caractéristiques principales du Synchrotron À Protons de Saclay et résultats
3010 obtenus lors de la mise en route, rapport CEA no.93, CEN-Saclay, 1958.
- 3011 26. Méot, F.: Zgoubi Users' Guide.
3012 <https://www.osti.gov/biblio/1062013-zgoubi-users-guide> Sourceforge latest version:
3013 <https://sourceforge.net/p/zgoubi/code/HEAD/tree/trunk/guide/Zgoubi.pdf>
- 3014 27. Foss, M.H., et al.: The Argonne ZGS Magnet. IEEE 1965, pp. 377-382, June 1965
- 3015 28. Klaisner, L.A., et al.: IEEE 1965, pp. 133-137, June 1965